Princeton Plasma Physics Laboratory

PPPL-5350

The Core Plasma Physics and Its Impacts on the FNSF

C.E. Kessel

January 2017

Prepared for the U.S. Department of Energy under Contract DE-AC02-09CH11466.

Princeton Plasma Physics Laboratory
Report Disclaimers

Full Legal Disclaimer

Trademark Disclaimer

PPPL Report Availability

Princeton Plasma Physics Laboratory:

http://www.pppl.gov/techreports.cfm

Office of Scientific and Technical Information (OSTI):

http://www.osti.gov/scitech/

Related Links:

U.S. Department of Energy

U.S. Department of Energy Office of Science

U.S. Department of Energy Office of Fusion Energy Sciences

The Core Plasma Physics Basis and its Impacts on the FNSF

C. E. Kessel[1], D. B. Batchelor[2], P. T. Bonoli[3], M. E. Rensink[4], T. D. Rognlien[4], P. Snyder[5], G. M. Wallace[3], S. J. Wukitch[3]

[1]Princeton Plasma Physics Laboratory, Princeton, New Jersey, USA
[2]Oak Ridge National Laboratory, Oak Ridge, Tennessee, USA
[3]Massachusetts Institute of Technology, Cambridge, Massachusetts, USA
[4]Lawrence Livermore National Laboratory, Livermore, California, USA
[5]General Atomics, La Jolla, California, USA

contact: ckessel@pppl.gov

Abstract

The FNSF core plasma physics is examined with detailed analysis to establish the basis for the reference configuration, R = 4.8 m, a = 1.2 m, Ip = 7.87 MA, and B_T = 7.5 T, q_{95} = 6, f_{BS} = 0.52, $\beta_N < 2.7$ established in ref [1]. Plasma equilibrium analysis is used to provide the CS/PF coil solution, and time-dependent free-boundary plasma evolution simulations are used to examined the integrated behavior into the relaxed plasma state. Ideal MHD stability is used to establish the pedestal height with EPED, and n=1 stability is assessed with PEST1. Heating and current drive are examined for negative ion neutral beams , lower hybrid, ion cyclotron and electron cyclotron systems. A combination of 50 MW NB, 30 MW LH, 20 MW ICRF and 20 MW EC is the reference. The energy confinement requirements are found to be modest to provide 100% non-inductive current, with $H_{98} \sim 1.1$-1.2, however, GLF23 predictions lead to H_{98} values ~ 0.65-0.8 in the absence of α and rotational stabilization. The impacts on the FNSF include the holes in the FW for the H/CD, the presence of tungsten conductors in the blanket during disruptions, and finding solutions for the CS magnet.

I. Introduction

The Fusion Nuclear Science Facility (FNSF) has a number of simultaneous missions it is attempting to address on the pathway to DEMO and a commercial fusion power plant, one of which includes ultra-long pulse plasmas with sufficient performance to provide the neutron environment for the fusion nuclear mission. The physics philosophy chosen for the FNSF [1] includes several features listed below,

- 100% non-inductive plasma current
- Normalized beta near the no-wall beta limit, but with the capability to exceed the no-wall beta limit
- Double null configuration
- Strong plasma shaping
- Densities below, but near the Greenwald density
- High radiated power divertor solutions

- Mitigated disruptions
- Heating and current drive sources are not down-selected
- Tungsten solid plasma facing material

Here the study is exploring, with detailed physics analysis, how the FNSF configuration could reach these requirements, and what the implications are for the plasma support systems and other systems in the FNSF. The systems analysis provides an operating point that is used to guide more detailed physics analysis. This simple zero to one-dimensional analysis includes energy and particle balance, as well as plasma radiation, bootstrap current, and fast particle beta, and determines several scalar parameters that characterize the plasma. The plasma parameters from the systems code for the reference operating point are given in Table 1. The plasma has a major radius of 4.8 m, minor radius of 1.2 m, with an elongation and triangularity at the x-point of 2.2 and 0.63, respectively. The plasma current is 7.87 MA, and the toroidal field is 7.5 T. The plasma operating point has a q_{95} of 6.0 and a bootstrap fraction of 52%, which requires $\leq$ 120 MW of injected power to drive the remaining 3.8 MA. The volume average density is 1.4×10^{20} /m^3, which corresponds to 90% of the Greenwald density limit. This high value is chosen to be power plant relevant based on many studies [2-5]. The total β_N is about 2.4, found to be at or below the beta limit from ideal MHD studies [5]. The alpha power for this case is 104 MW, with 57 MW of radiative losses from bremsstrahlung, line and cyclotron radiation.

The paper will examine the poloidal field coil solution, time-dependent simulations of the plasma evolution to steady state, ideal MHD for peeling-ballooning modes and n= 1kink mode, heating and current drive, and conclude with a discussion of implications for the FNSF of plasma physics features.

Table 1. Plasma parameters from the Systems Code and from TSC [6] 1.5D simulations.

	Systems Code	TSC bT/pn	TSC bT/bn	TSC mT/pn	TSC mT/bn	TSC pT/pn	TSC pT/bn
Ip, MA	7.87	7.90	7.90	7.90	7.90	7.90	7.90
I_{CD}, MA	3.78	3.42	3.14	3.44	3.16	3.60	3.31
I_{LH}, MA		1.07	0.96	1.05	0.94	1.04	0.93
I_{FW}, MA		0.40	0.40	0.44	0.44	0.50	0.50
I_{NB}, MA		1.73	1.56	1.71	1.54	1.79	1.61
I_{EC}, MA		0.22	0.22	0.24	0.24	0.27	0.27
I_{BS}, MA		4.48	4.87	4.52	4.89	4.62	4.98
B_T, T	7.5	7.5	7.5	7.5	7.5	7.5	7.5
$l_i(1)$	0.7	0.73	0.66	0.76	0.70	0.80	0.74
q(0), q_{95}	6.0	1.55, 5.7	1.72, 5.7	1.56, 5.7	1.72,5.7	1.65, 5.8	1.63. 5.7
n/n_{Gr}	0.9	0.86	0.92	0.87	0.91	0.85	0.91
W_{th}, MJ	170	183	202	184	203	189	208
n(0), x10^{20} /m^3	1.93	1.95	1.95	1.95	1.95	1.95	1.95

$\langle n \rangle_v$, $x10^{20}$ /m^3	1.38	1.32	1.46	1.32	1.43	1.30	1.43
$n(0)/\langle n \rangle$	1.4	1.48	1.33	1.48	1.36	1.50	1.36
β_N^{th}	2.2	2.40	2.65	2.39	2.66	2.49	2.72
f_{BS}	0.52	0.57	0.62	0.57	0.62	0.58	0.63
τ_E, s	0.86	1.1	1.14	1.09	1.14	1.10	1.14
$H_{98(y,2)}$	0.99	1.1	1.13	1.13	1.18	1.13	1.20
$T_{e,i}(0)$, keV	23.7	24.0, 21.6	24.1, 22.1	26.3, 24.0	26.5, 24.5	30.0, 26.2	30.4, 26.9
$T(0)/\langle T \rangle$	2.6	2.2	2.2	2.43	2.43	2.66	2.69
$T_{e,ped}$, $T_{i,ped}$ keV		4.3, 4.0	4.3, 4.0	4.4, 4.0	4.3, 4.0	4.4, 4.0	4.3,4.1
Z_{eff}	2.4	1.78	1.78	1.78	1.78	1.78	1.78
P_{alpha}, MW	104	86.4	104	89	105	93	109
P_{CD}, P_{total}, MW	121, 129	120, 120	120, 120	120, 120	120, 120	120, 120	120, 120
P_{LH}, MW		30	30	30	30	30	30
P_{IC}, MW		20	20	20	20	20	20
P_{NB}, MW		50	50	50	50	50	50
P_{EC}, MW		20	20	20	20	20	20
P_{brem}, MW	24.6	14.5	18.0	14.5	18.0	14.2	17.0
P_{cycl}, MW	1.9	5.5	6.0	6.0	6.0	6.7	7.0
P_{line}, MW	29.3	21.0	23.8	21.0	24.0	20.8	23.8
$P_{L\text{-}H\ threshold}$, MW		89.2	104.3	88.0	104.3	88.9	109
P_{net} / $P_{L\text{-}H}$		1.86	2.20	2.36	2.17	1.92	2.10
n_{He}/n_e	0.0245	0.057	0.059	0.057	0.059	0.057	0.06
n_{DT}/n_e	0.87	0.85	0.845	0.85	0.84	0.84	0.84
n_{Ar}/n_e	0.0045	0.002	0.002	0.002	0.002	0.002	0.002
n_W/n_e	0	1.0e-5	1.0e-5	1.0e-5	1.0e-5	1.0e-5	1.0e-5

bT = broad temperature, mT = medium peakedness temperature, pT = peaked temperature, bn = broad density, pn = peaked density

II. Poloidal Field and Central Solenoid Determination

The inboard radial build derived from the nuclear analysis and systems analysis places the central solenoid (CS) coil at a center radius of 0.85 m, with a thickness of approximately 0.4 m. The Tokamak Simulation Code [6] (TSC) analysis shows that ~ 90-100 Wb are required to rampup the plasma current over 60 s, from 0.5 MA to 7.9 MA. The plasma begins as a nearly circular limited plasma with large aperture, and is grown vertically to full size and shape. The plasma diverts at ~ 10-12 s into the rampup and simultaneously has largely reached full size. Heating begins at 20 s and steps from 5 – 10 MW through the rampup.

Table 2. Fiducial equilibria parameters for the FNSF with corresponding coil currents.

Ip, MA	0.0	0.5	1.0	1.5	2.25	4.5	6.75	7.87	7.87
$l_i(1)$		1.13	1.0	1.0	1.1	1.0	1.0	1.0	0.9
β_N		0.07	0.08	0.08	0.5	0.5	0.6	1.3	2.5
Ψ, Wb	-50	-40	-30	-20	-10	10	30	50	50
lim/div		lim	lim	lim	div	div	div	div	div
Time, s	0	1.5	3.5	6.0	10.0	20.0	35.0	60.	70.
CS1	10.6	8.40	4.63	2.20	3.86	-4.59	-15.7	-26.5	-21.6
CS2	16.0	12.9	9.53	5.92	1.55	-4.10	-9.56	-12.5	-9.70
CS3	19.7	16.0	13.8	10.0	2.45	-0.51	-6.51	2.23	2.47
CS4	18.2	14.8	13.8	11.4	8.74	7.14	8.18	8.74	7.16

CS5	13.5	11.1	10.7	9.59	13.9	13.1	13.0	8.38	6.12
PF1	2.43	1.99	1.97	1.92	3.89	4.03	3.68	1.36	0.88
PF2	3.59	2.95	2.90	2.85	4.96	5.44	4.99	1.65	1.18
PF3	4.66	3.82	3.73	3.67	4.63	5.57	5.25	1.68	1.52
PF4	2.68	2.21	2.01	2.03	-2.58	-1.28	0.0	2.06	3.45
PF5	0.74	0.62	0.45	0.61	-1.10	-0.27	1.24	4.20	5.27
PF6	-2.54	-2.11	-2.05	-1.71	8.19	7.17	6.63	4.72	3.04
PF7	1.32	1.01	0.48	-0.40	-6.94	-8.82	-11.2	-12.7	-12.9

A series of fiducial plasma equilibria were established along the plasma pulse, excluding rampdown, which was not modeled. Table 2 gives these fiducial states, and their parameters, and approximate times in the pulse. After the envelope for the toroidal field coil and its support structure was established, the poloidal field coils could be placed outside. Due to the horizontal maintenance approach used in the FNSF, no PF coils are allowed on the outboard side since the maintenance port occupies this region. Fig. 1 shows the CS and PF coils along with the plasma, vertical stabilizing plates, and vertical feedback coils, in the TSC model. The distance of the CS and PF coils from the plasma is clearly visible, and is the result of more conservative TF coil nuclear damage limits and heating, exclusion of water inside and including the vacuum vessel, and the desire to keep the facility small. The coil currents at the fiducial states are shown in Fig. 1, with 2 different shifts to the flux state. The coil sizes and locations are given in Table 3. This coil geometry and waveforms (as pre-programming) are used in the time-dependent simulations and the mechanical analysis of the TF/CS/PF coils.

Table 3. CS and PF Coil positions and cross-sections.

CS/PF coil	R, m	Z, m	ΔR, m	ΔZ, m
CS1*	0.85***	0.4	0.40	0.80
CS2	0.85	1.2	0.40	0.80
CS3	0.85	2.0	0.40	0.80
CS4	0.85	2.8	0.40	0.80
CS5	0.85	3.6	0.40	0.80
PF1**	1.25	5.35	0.50	0.50
PF2	1.95	5.85	0.60	0.60
PF3	2.65	6.00	0.61	0.61
PF4	4.40	6.30	0.42	0.42
PF5	5.15	6.25	0.59	0.59
PF6	7.25	5.80	0.73	0.73
PF7	8.75	5.00	0.92	0.92

*assuming 75 MA/m^2 current density, HTSC

**assuming 15 MA/m^2 current density, square coils, and LTSC

***a bucked and wedged design can move the CS coils out and reduce their currents significantly [7].

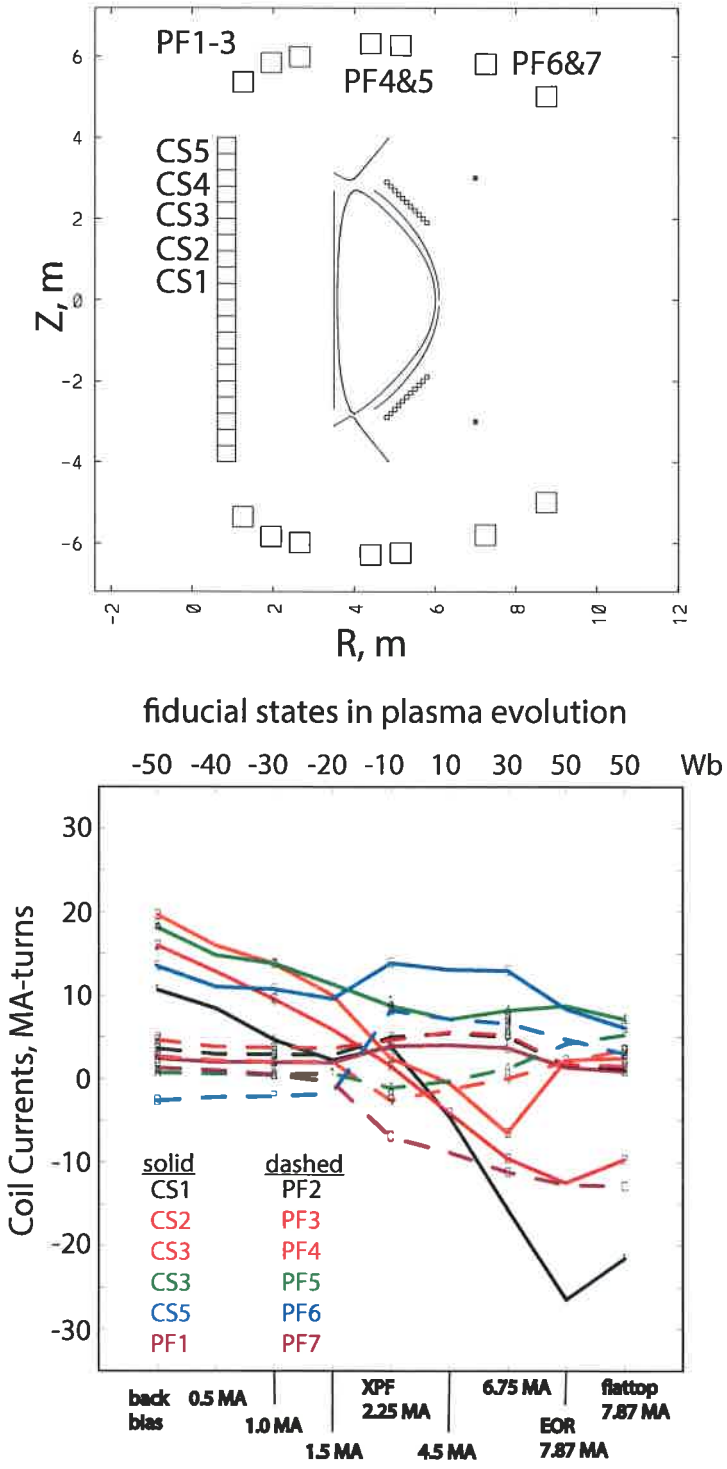

Figure 1. The central solenoid (CS) and poloidal field (PF) coils, plasma, limiters, passive stabilizer shells, and internal vertical feedback coils (left). The coil currents for the fiducial equilibria from back bias through to the start of burn in the flattop, for the reference back bais of -50 Wb.

III. Time Dependent Simulations

TSC is used to simulate the free-boundary time-dependent behavior of the plasma from its limited starting point at 0.5 MA plasma current to well into the flattop when all profiles have reached a steady state. The simulation includes 2D equilibrium and Ohm's Law evolution with 1D transport of energy, while the density is prescribed as a function of time. The Coppi-Tang semi-empirical model [7,8] is used, and the GLF23 theory based model [9,10] is also examined. The EPED pedestal model [11] results for the FNSF configuration are programmed in the TSC simulation and constrain the pedestal pressure. The simulations includes bootstrap current with the Sauter model [12], plasma radiation (cyclotron, bremsstrahlung and line assuming coronal equilibrium), fusion reactions and He production, impurities (Ar and W), and feedback control systems for the plasma position, shape and current. The goal of the simulations is to recover, to the extent possible, the systems code operating point, simultaneously meeting some global parameters including 100% non-inductive plasma current, ~ 100 MW of alpha power, and $\leq$ 120 MW of auxiliary power. Detailed heating and current drive analysis done separately are used to identify the CD efficiency to enforce and the deposition profile to represent that source in TSC. These are described in Section V.

Table 1 provides six TSC cases and several parameters compared with the systems code solution. Figure 2 presents the evolution of the plasma during early rampup to x-point formation, and then the relaxed plasma boundary in flattop. The plasma is predominantly grown vertically since the plasma-facing boundary is close by. The x-point formation allows heating to begin as the strike flux lines enter the divertor and are actively controlled to remain there. The passive stabilizing plate on the outboard of the plasma is clearly seen, and the vertical position feedback coils which would lie on the back of the structural ring. This vertical stability and control solution follow the guidelines described in ref [13], which include tungsten passive stabilizers and in-vessel feedback control coils. The plasma in flattop has a lower squareness than those in the rampup phase, and the minimum SOL distance from the plasma boundary to the wall is 10 cm. Fig. 3 shows the flattop plasma profiles for the broad temperature and broad density case. Figs. 4, 5, and 6 show the plasma current, density, central temperature, internal self-inductance, volt-seconds and central safety factor, and powers as a function of time for this reference case. These results are typical of all six cases. The plasma heating in the rampup phase is accomplished with ICRF or EC at ~ 5 MW, and LH is introduced at ~ 5 MW also. At the end of the plasma current rampup, 20 MW of EC, 20 MW of ICRF, and 15 MW of LH are injected simultaneously to enter the H-mode. The threshold power [14] is ~ 40 MW at the end of the ramp. As the density rises the NB is injected in two steps, 25 MW and then the full 50 MW, 10 s and 20 s after the end of the current rampup, in order to avoid shine-through at lower densities. The H-mode threshold power in the flattop reaches ~ 90 MW, and with the alpha power contribution, the ratio of $P_{net}/P_{LH,thr} > 1.8$. Overall the plasma takes several hundred to 1000 s to relax, mainly due to the high central temperature and decay of inductive current originally introduced in the rampup phase. It is expected that the rampup and relaxation phases can be optimized to reduce the inductive current generation and minimize the departure of the plasma current density profile from the flattop configuration.

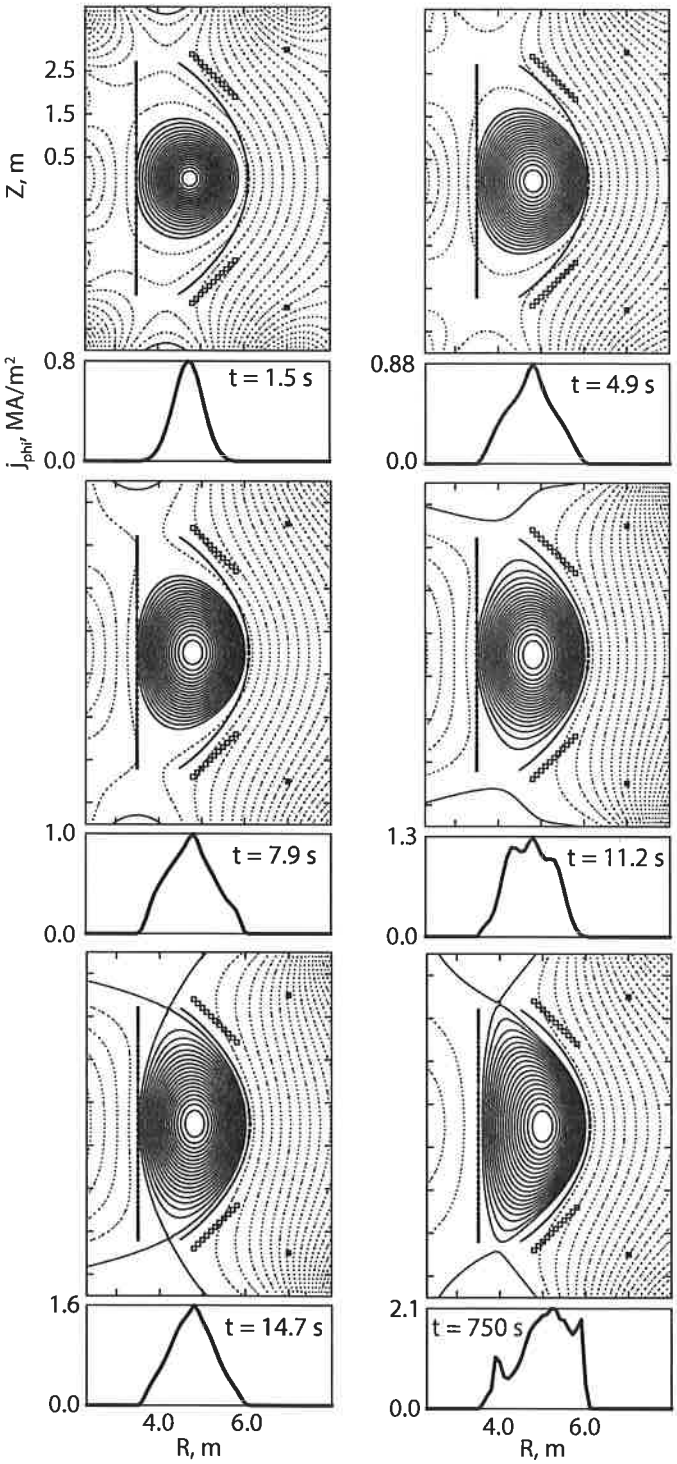

Figure 2. The poloidal magnetic flux for a series of plasmas in the early rampup leading to x-point formation. The final plasma is the relaxed plasma in flattop.

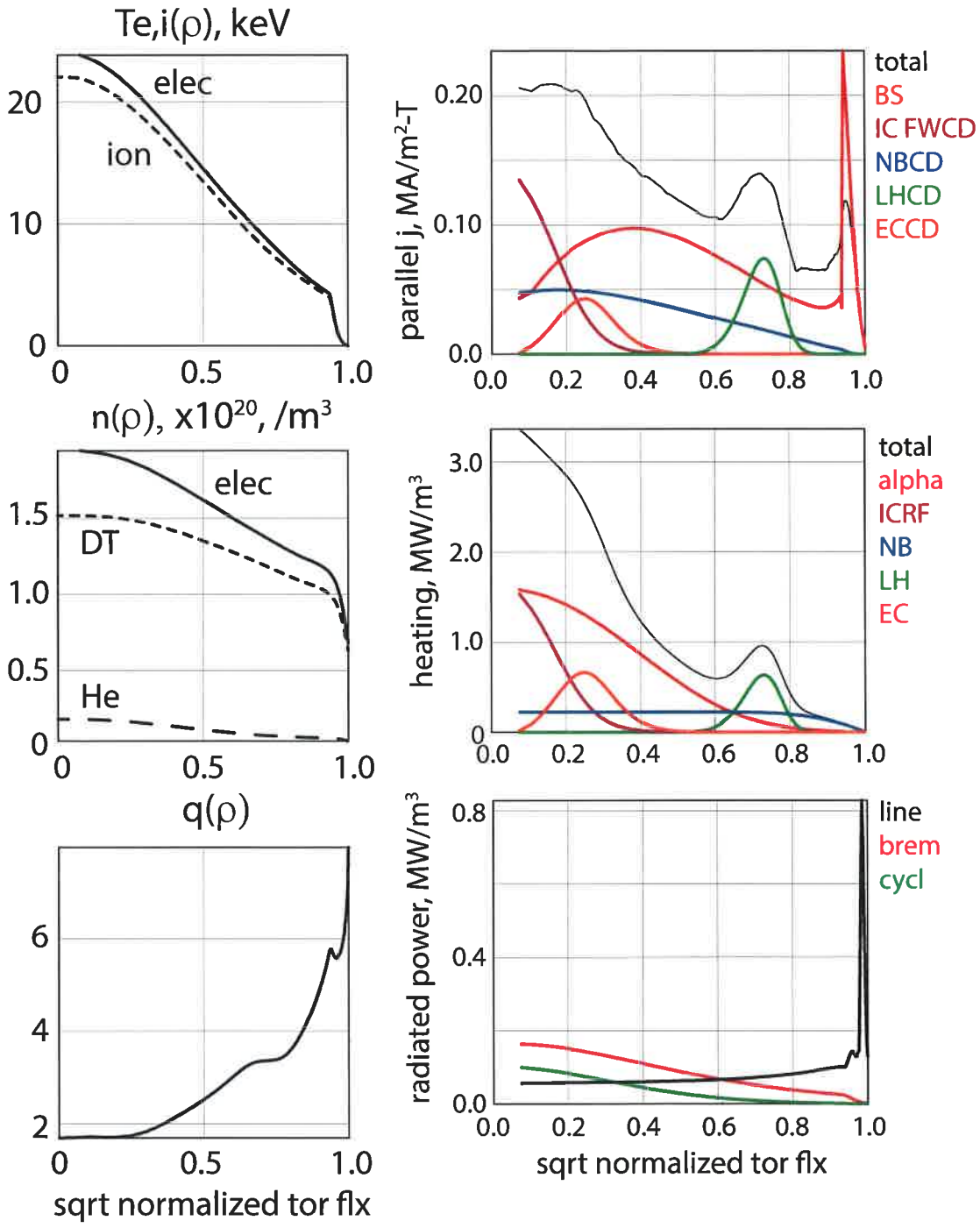

Figure 3. Temperature, density, safety factor, current density and power deposition, and radiated power profiles are shown for the broad density/broad temperature case.

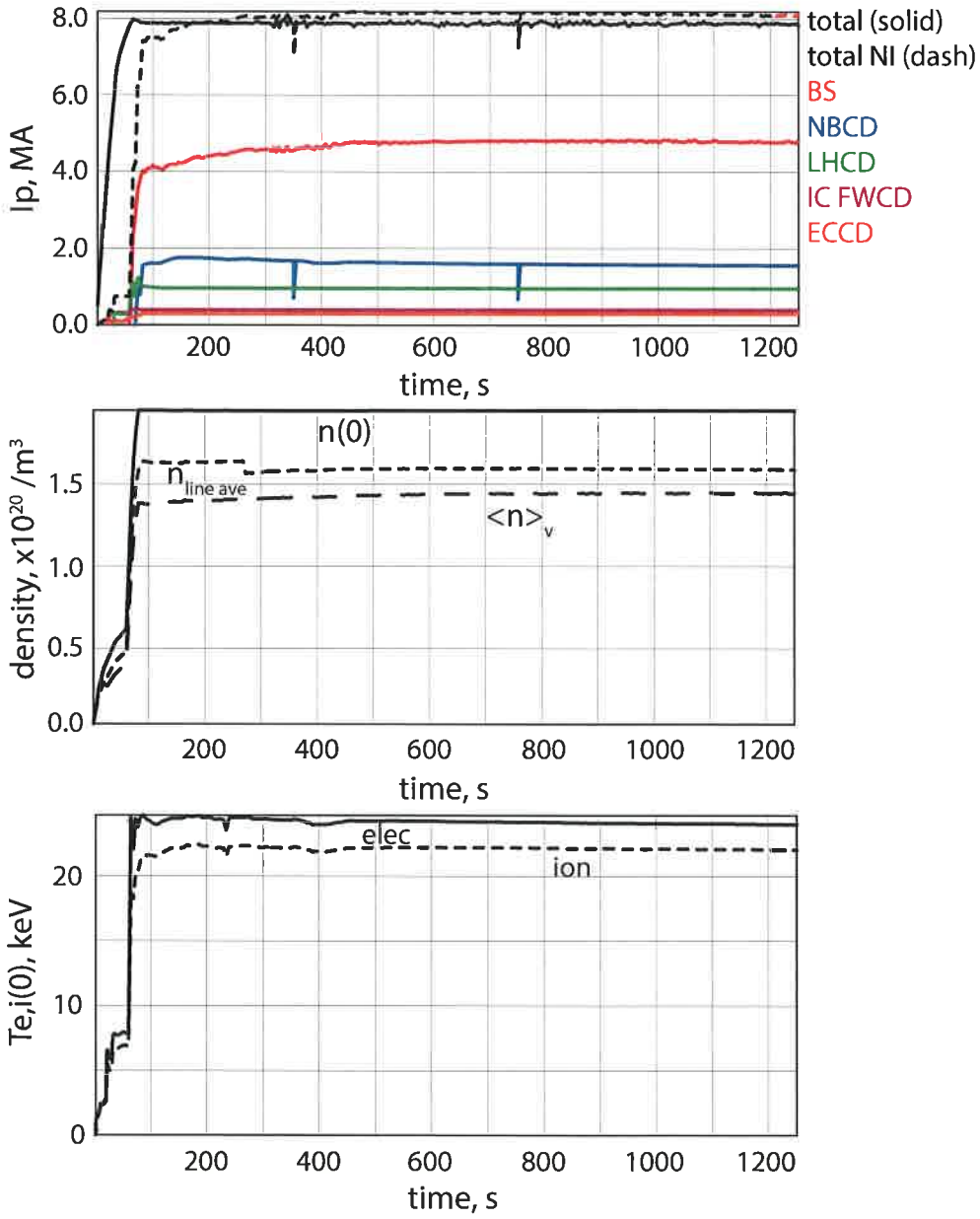

Figure 4. Time histories of the plasma current and its contributions, the density, and central temperature, for the broad density / broad temperature case. The plasma current is slightly overdriven by ~ 200 kA.

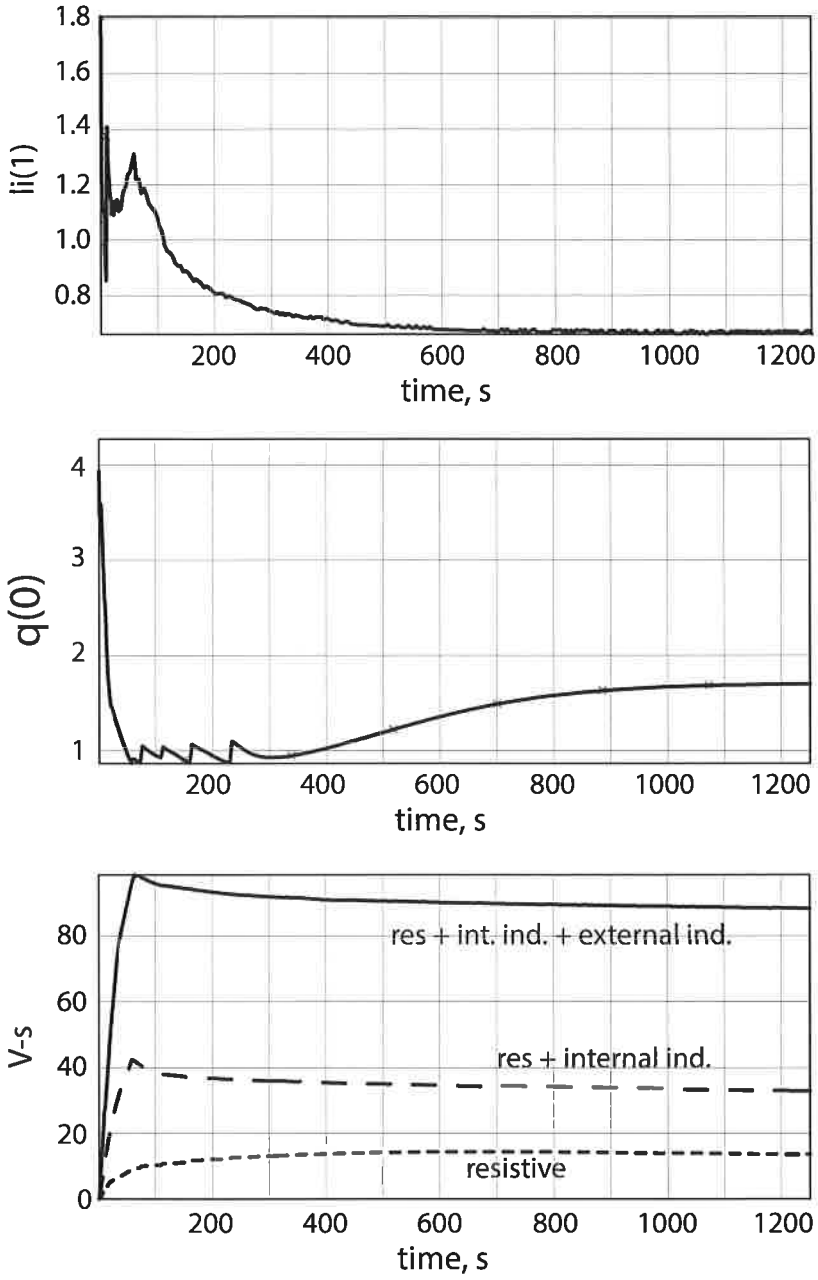

Figure 5. Time histories of the internal self-inductance, central safety factor and volt-second. The V-s are from the Axial method. Sawteeth are evident in the early phase after rampup, but disappear as the current profile relaxes. All cases reach q(0) ~ 1, but have different durations before rising as the configuration relaxes.

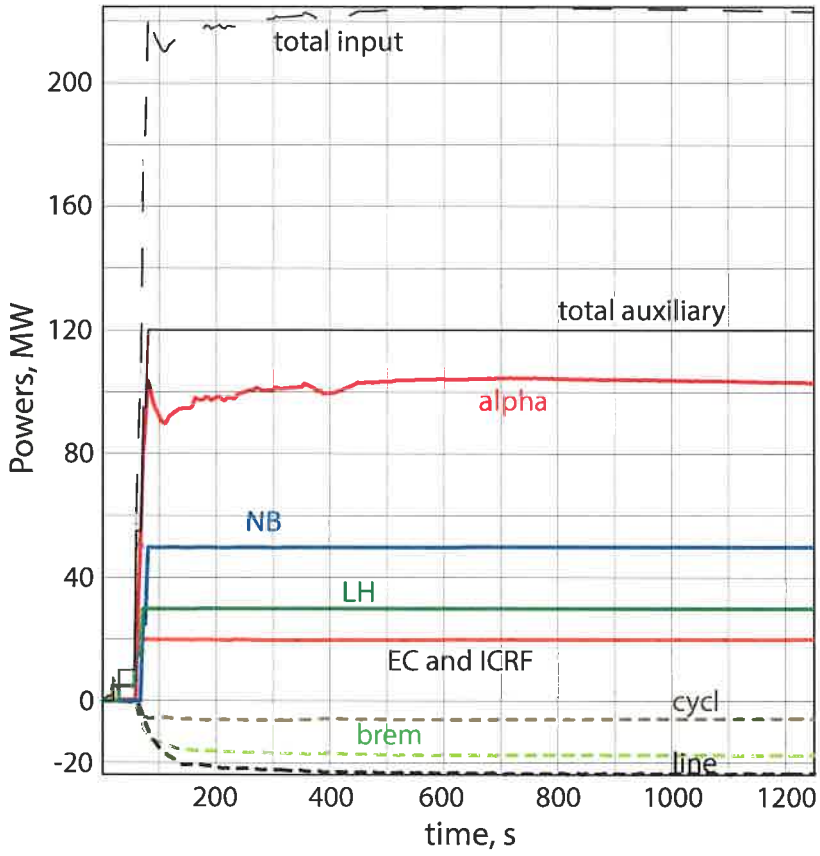

Figure 6. Time histories of the various power terms. The alpha power reaches ~ 100 MW. The ICRF curve is hidden by the EC curve since they have the same powers injected.

The six TSC cases are varying the combinations of temperature and density profiles shown in Fig. 7. The alpha powers ranged from 86-109 MW. All the TSC cases were required to reach ~ 100% non-inductive plasma current, and so the Coppi-Tang (CT) transport was adjusted globally to obtain this. The resulting global energy confinement factor H_{98} turned out to be generally higher than predicted by the systems code, 1.1-1.2 versus 1.0. The driven currents shift somewhat with the change in temperature and density profiles, the stored energies vary from 183-208 MJ, and the internal self-inductance ranged from 0.66 to 0.8. All cases have assumed 0.2% argon (n_{Ar}/n_e) and 0.001% tungsten (n_W/n_e). The thermal diffusivity for the CT model is given below,

$$\chi_{CT} = \chi_o \chi_{CTo} f_{CT}(\rho), \quad 0 < \rho < \rho_{ped}$$

$$\chi_{CT} = \chi_o \chi_{CTo} f_{CT}(\rho_{ped}) f_{EPED} f(c_m\{\rho - \rho_{ped}\}/\{\rho_{sep} - \rho_{ped}\}), \qquad \rho_{ped} < \rho < \rho_{sep}$$

Here χ_o is used to adjust the overall transport, while $\chi_{CTo} f_{CT}(\rho)$ is from the model [7]. From the pedestal top location to the separatrix, the f_{EPED} reduction is applied and an

additional factor to make the thermal diffusivity grow strongly between the pedestal and the separatrix to reproduce experimental observations of the temperature fall off and low separatrix temperatures.

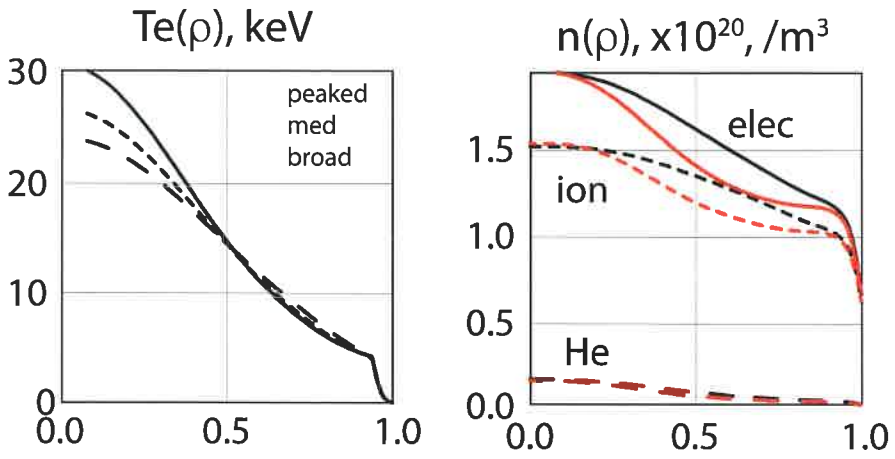

Figure 7. Temperature and density profiles used in the time-dependent simulations with the Coppi-Tang model to examine the impacts of changes on the alpha power and energy confinement required to obtain 100% non-inductive plasma current.

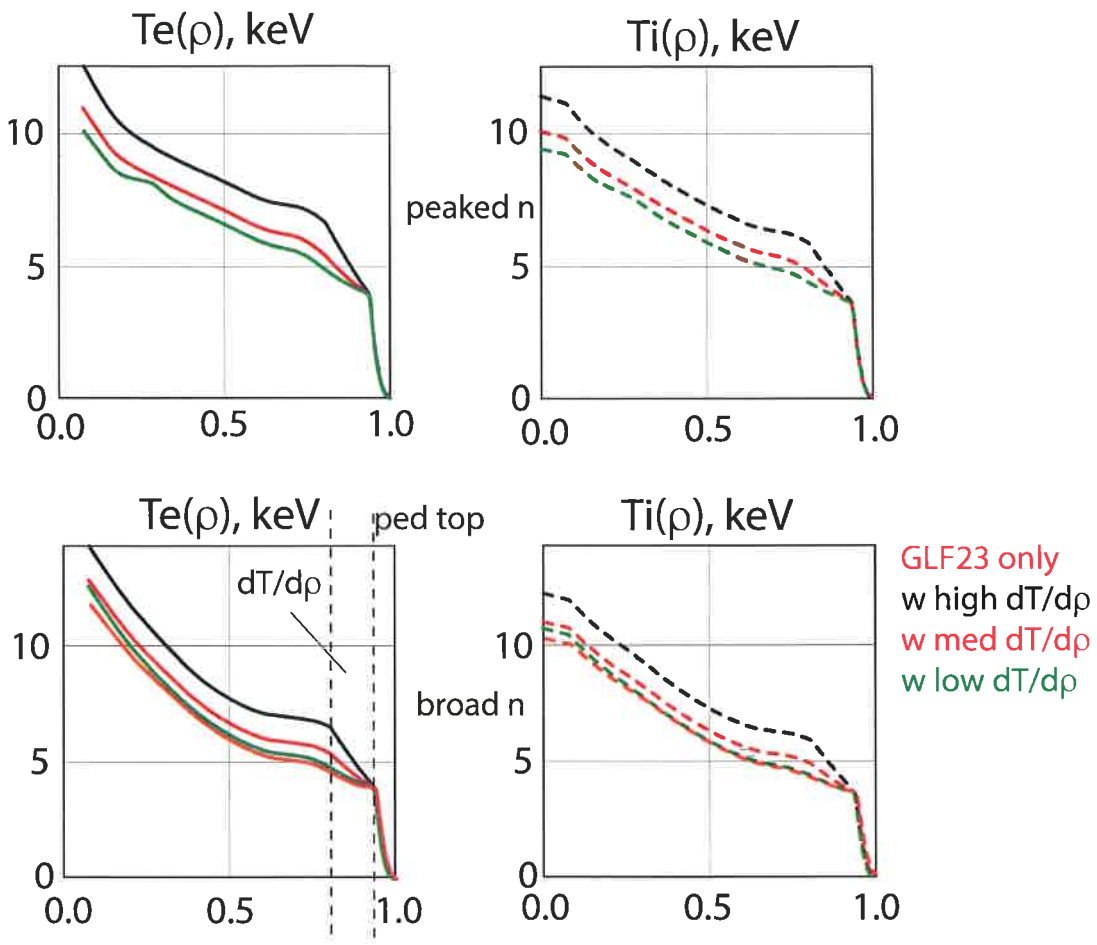

Figure 8. The temperature profiles from the GLF23 transport model for the FNSF operating point, with the same pedestal derived from EPED, for broad and peaked density profiles, and different assumptions about the temperature profile just inside the pedestal top. The pedestal top and dT/dρ are denoted by the vertical dashed lines.

The GLF23 theory based model [9,10] for energy transport was applied to see the predictions from this model. The α-stabilization term (associated with the Shafranov shift) was turned off due its optimistic predictions, and the plasma rotation term was not effective for low rotation speeds anticipated. The ExB shear stabilization factor coefficient was set to its reference value of 1.35. Several cases were run to examine the impact of Z_{eff}, n(0)/<n>, and n(ρ) magnitude, however, all GLF23 predictions were pessimistic. Higher density was favored by the model and led to the highest alpha powers for this model of 50-60 MW. However, these densities severely reduced the external driven current. The resulting H_{98} factors were in the range of 0.7-0.85. The Z_{eff} was lowered in order to avoid very high radiated power resulting from the slow temperature rise inside the pedestal with the GLF23 model. Since it has been suggested that the GLF23 model is not applicable to the region of the plasma just inside the pedestal top, GLF23 was not applied from the magnetic axis to the pedestal top. Instead, a fixed temperature profile was enforced between $0.8 < \rho < \rho_{ped}$, and the EPED defined pedestal

was used from the pedestal to the separatrix as before. This can be seen in Fig. 8, which shows the series of temperature profiles for the peaked and broad density (with reference magnitude $n(0) = 1.95x10^{20}$), and three different temperature gradients between $\rho = 0.8$ and ρ_{ped}. The lowest temperature gradient case is nearly identical to the GLF23 case itself. The higher temperature gradient case does result in higher temperatures across the profile. The alpha powers ranged from 16-20 MW at the low gradient (or GLF23 by itself) to 25-35 MW for the highest gradient. Simultaneously the non-inductive current fractions obtained were 0.53 to 0.67, and H_{98} values of 0.65 to 0.8, from the lowest to the highest temperature gradients. For all these cases the electron and ion pedestal temperatures were 4.0 and 3.7 keV, respectively, due to lower Z_{eff} of 1.35. Further examination of the theory based transport prediction is needed to better understand if there are specific characteristics of these low fusion gain plasmas, with high injected power for CD, that contribute to a low prediction for energy confinement.

IV. Ideal MHD Stability

IV.1. Peeling Ballooning Stability

The EPED peeling-ballooning stability analysis [11] was used to establish the pedestal pressure as a function of the pedestal density and Z_{eff}. This constraint is important to core plasma transport as a boundary condition, it sets the edge bootstrap current for the ideal MHD stability, and is used to determine parameters associated with ELMs. The correlation for the top of the pedestal derived from the analysis is given by

$$P_{ped,top}\ (kPa) = 59.4 + 5.94\ [\ n_{19,ped}\ (Z_{eff,ped})^{1/2}\ ]$$

$$\Delta_{psi,ped\text{-}top} = 0.0053 + 0.0014\ [n_{19,ped}\ (Z_{eff,ped})^{1/2}\ ]$$

Table 4 provides some pedestal temperatures with different density at $Z_{eff} = 2.4$, and resulting information relevant to ELMs based on these pedestal values. The formulations for the ELM parameters [15] are based on experiments to provide guidance for ITER. The relationship used for the integrated power width is from ref [16]. These ELM heat flux predictions are used in the transient thermo-mechanics analysis reported in [17]. This EPED correlation was subsequently programmed in TSC and enforced for the time-dependent simulations shown here. The pedestal information was also used to constraint the equilibrium and ideal MHD analysis reported here.

Table 4. ELM characteristics derived from the EPED pedestal parameters for the FNSF.

W_{ped}, MJ	60	67	74	87
P_{ped}, kPa	151	170	188	220
T_{ped}, keV	4.7	4.4	4.2	4.0
n_{ped}, $x10^{20}$ /m^3	1.0	1.2	1.4	1.74 (= n_{Gr})
ΔW_{ELM}, MJ	12.0	13.4	14.8	17.4
$\Delta W_{ELM,div}$, MJ	6.0	6.7	7.4	8.7

$\Delta W_{ELM,div}^{rise}$, MJ	2.4	2.7	3.0	3.5
$\Delta W_{ELM,div}^{rise}$, MJ per divertor (65%)	1.56	1.74	1.92	2.26
$\tau_{\|\|}$, ms	0.3	0.31	0.32	0.33
Rise time ($2x\tau_{\|\|}$), ms	0.6	0.62	0.64	0.66
$A_{ELM,div}^{OB}$, m^2	1.32**			
$A_{ELM,div}^{OB}$, m^2, x4	5.28			
$q_{ELM,div}^{OB}$, MW/m^2	1970	2126	2272	2594
$q_{ELM,div}^{OB}$, MW/m^2 (expanded area)	492	532	568	649
f_{ELM}, Hz	4.4	3.9	3.6	3.0
Inter-ELM power	125	125	124	125
$q_{div,OB}^{peak}$ (inter-ELM), MW/m^2	7.6	7.6	7.5	7.6
$q_{div,IB}^{peak}$ (inter-ELM), MW/m^2	2.77	2.77	2.75	2.77

*compared to the steady state peak heat flux of 10.0 MW/m^2

**Fundamenski formulation for λ_{int}

IV.2. n=1 Stability Analysis

The plasma physics strategy for the FNSF is to guarantee that the facility can reach its mission with the lower beta operating regime, but be capable of taking advantage of operating above the no-wall beta limit at least to some level. This is chosen to address the need for robust plasmas as the pulse duration reaches days to weeks. Meanwhile, this also allows the increase of the neutron wall loading, bootstrap current fraction, operating space, and higher fusion gain, if higher beta's can be reached. In order to take advantage of higher beta operation it requires feedback control of error fields and/or RWM fields, plasma rotation, and or kinetic stabilization via fast particle populations. Ideal MHD analysis is performed using the JSOLVER [18] flux coordinate equilibrium code, the BALMSC [19] high-n ballooning stability code, and PEST1 [20] low-n kink stability code. This is used to identify the no-wall beta limit, and what the impact of a conducting wall could have on this beta limit. All configurations examined were ballooning stable. For plasma in this beta range the n=1 external kink mode is the most unstable, and this is examined here.

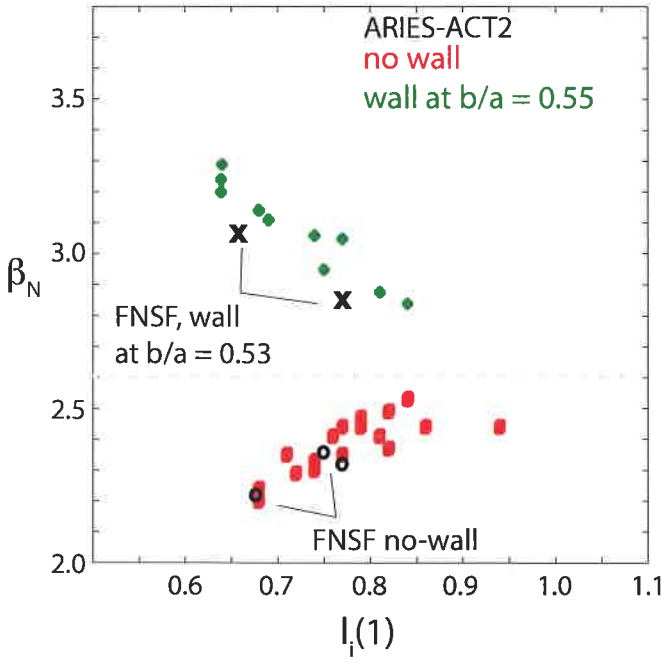

Figure 9. Normalized beta limit for the n=1 kink mode versus the internal self-inductance, showing the results for the ARIES-ACT [ ] study both no-wall and with a conducting wall at 0.55 times the minor radius. The FNSF configurations agree with this data.

Since the plasma has approximately 50% bootstrap current, the remaining plasma current must be driven by external current drive sources, such as neutral beams (NB), lower hybrid (LH), ion cyclotron fast wave (ICRF), or electron cyclotron (EC). The TSC configuration can be reproduced in the JSOLVER equilibrium code, and the CD components can be imitated to allow adjustments of pressure, higher or lower, in order to find the beta limits. The CD components are added to the self-consistent bootstrap current, while the density and temperature profiles are prescribed by the TSC simulations. The beta limit can be determined by varying the pressure and adjusting the external current drive so that the total plasma current is fixed to the FNSF operating point value. Shown in Fig. 9 is β_N versus li(1), with the results of the ARIES-ACT2 plasma study in red (no wall beta limit) and green (with wall beta limit), and the FNSF cases shown in black. Since the ARIES-ACT2 operating point was also approximately at the no wall beta limit, the no wall beta limits for 3 FNSF cases largely confirm the previous trend. The NB driven current profile for the FNSF is broader than the one determined for the ARIES-ACT2, and is making the higher li(1) values inaccessible. The pedestal is also generating a relatively large bootstrap current. The three cases assume current driven by; two with NB and IC only, and one with NB, IC, and LH. If no wall is assumed the maximum normalized beta's are 2.31 and 2.35 (NB and IC), and 2.23 (NB, IC and LH). If a conducting wall is assumed at the back of the breeding blanket zone, which is 1.2 m away from the plasma boundary, there is virtually no improvement in the beta limit. If a conducting wall is placed at the halfway point in the breeding blanket, ~ 0.53 times the minor radius and measured from the plasma boundary, the beta limits rise from 2.23 to

3.06, and 2.31-2.35 to 2.84. The stabilizing kink shells need to be located where they can be firmly mounted to structure, so it is possible from the outboard blanket design to place such shells at ~ 0.33a, 0.53a, and 0.74a. Stability analysis including kinetic stabilization and/or rotation and RWM feedback could extend these results [21-23].

V. Heating and Current Drive

Since demonstrations on a burning plasma tokamak at 10's MW levels is lacking, the four main heating and current drive sources were not down-selected. Lower hybrid (LH), negative ion neutral beams (NB), ion cyclotron (IC) and electron cyclotron (EC) were considered for the FNSF flattop conditions.

V.1. Ion Cyclotron, Fast Wave

The ICRF was examined as a function frequency based on the toroidal field at the plasma geometric center of 7.5 T, in the range of 68 – 92 MHz, targeting the region of the $2\omega_{c,T}$ = 76 MHz. The presence of fast alpha particles from fusion reactions, and possible fast deuterons from neutral beam were included. The $2\omega_{c,D} = 2\omega_{c,He}$ (= 114 MHz) resonance region is avoided due the combination of fast and thermal deuterium and helium in the plasma. Experiments on TFTR and JET [24,25] have demonstrated the effectiveness of the second harmonic tritium resonance heating, which is also a primary heating scheme for ITER. A minority fraction of He3, $\omega_{c,He3} = 2\omega_{c,T}$, can enhance the ion heating while avoiding the deuterium/helium resonances, and may be accessible in a FNSF or other fusion nuclear device due to the decay of tritium which may need be separated from the tritium before freezing into pellets. TORIC5 [26,27] was used to simulate the ICRF power deposition in the flattop FNSF plasma. Shown in Fig. 10 is the electron and tritium absorbed power fractions, and the fast wave (FWCD) current drive efficiency as a function of the frequency.

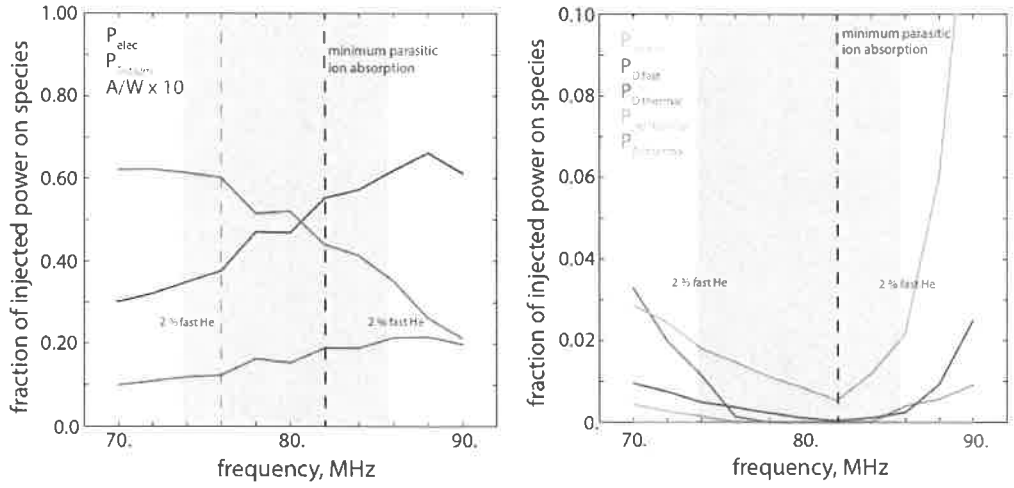

Figure 10. Fraction of power absorbed on electrons and tritium, and the fast wave current drive efficiency (left), the fraction of power absorbed on other ions (right), He, D, and Ar.

The tritium absorption reaches as high as > 60% around and below its cold plasma resonance. The electron heating, and subsequently the FWCD, continue to increase over the range of 70-88 MHz, reaching 65% absorption and 0.021 A/W, or nRI_{CD}/P_{CD} of 0.2 A/W-m^2, respectively. The ion absorption among the fast alpha particles and NB deuterons begins rising strongly above 82 MHz due to Doppler broadening of their cold resonance at 114 MHz. Thermal argon also rises above 82 MHz as its cold resonance is approached (103 MHz). As the frequency is lowered the deuterium and He, both thermal and fast, rise again more slowly, as their fundamental resonances are approached. The fast alpha absorption dominates the parasitic ion absorption, and a minimum in fast alpha absorption occurs at 82 MHz, with about 0.7% absorbed power. This is also a minimum for all ions, except tritium. Fig. 10 shows the frequency band bounded by 2% fast alpha absorption, which occurs from about 74 to 84 MHz. Depending on the tolerable level of alpha absorption of the ICRF power, the frequency could be chosen 80-84 MHz to maximize the FWCD efficiency and minimize the parasitic ion absorption. Fig. 11 shows the electron and tritium heating, and fast wave current driven at 84 MHz and 76 MHz (the cold tritium resonance). Most significant is the shift in tritium heating location, with only minor changes in the electron heating and current drive profiles. The shift in tritium absorption location is to the high field side. For this derived current drive efficiency, 20 MW of injected power would drive ~ 0.4 MA, located on-axis with a narrow profile. This is advantageous for providing current where the bootstrap current is decreasing to zero, and avoids high central safety factor values. ICRF power is also useful in the current rampup and early heating to burn.

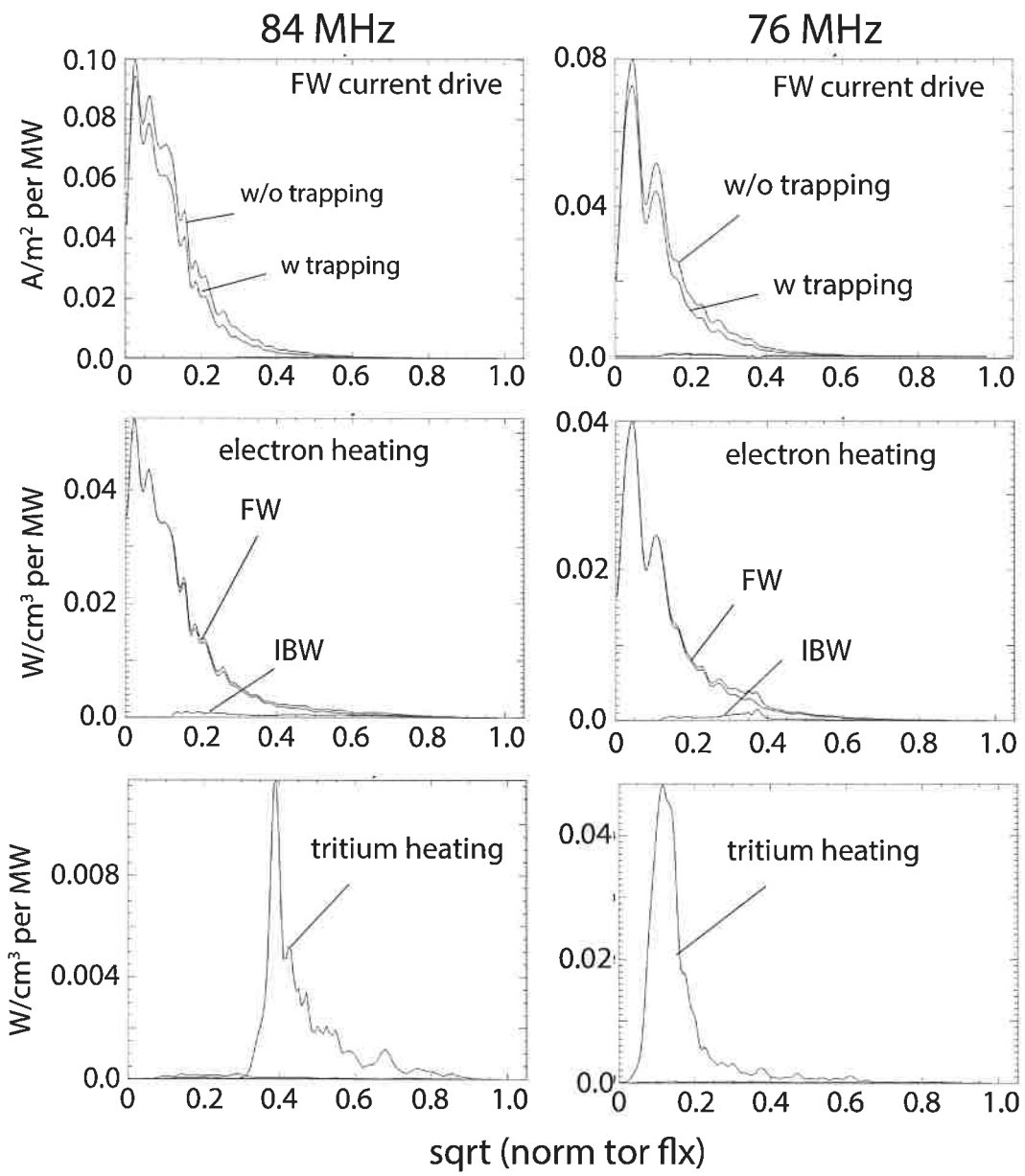

Figure 11. Profiles of the tritium absorbed power, electron absorbed power, and fast wave current drive for 84 and 76 MHz.

V.2. Lower Hybrid

The lower hybrid provides current drive in the outer half radius of the plasma. The launched frequency is chosen to be 5 GHz to avoid alpha particle absorption that would occur at lower frequencies and to avoid very narrow waveguides which occurs at higher frequencies. The launch location was varied from 0 (midplane), 42.5 and 60 degrees on the outboard side (low field side), and at 180, 195, and 225 degrees on the inboard side (high field side). The launched parallel index of refraction was varied from $n_{||} = 1.4$ to 2.5 to establish the current drive efficiency in the plasma. The forward positive (co-Ip) lobe

carried 75% of the power, and the negative directed lobe (cntr-Ip) carried 25% of the power. This weighting is typical of passive-active multi-junction (PAM) waveguides. The negative lobe is simulated to be at $n_{||}$ = -6.0. The GENRAY-CQL3D [28,29], which includes 2D Fokker-Planck treatment of the electron distribution function, was used to determine the power and current drive deposition, and more detail is reported elsewhere [30].

Shown in Fig. 12 is the driven current for 30 MW of injected power as a function of the minor radius, for the optimum LFS (42.5 degrees) and HFS (225 degrees) launch locations. For low field side (LFS) launch, the driven current increases significantly when the launch is moved above the midplane. The characteristic shape of CD efficiency versus launched $n_{||}$ shows the accessibility limits at low $n_{||}$, where the waves are converted to fast waves and ultimately damp at lower temperatures with lower CD efficiency. At high $n_{||}$ the waves damp, as slow waves, at progressively larger radii where the electron temperature is lower, which can be understood from the expression for the maximum temperature for electron Landau damping, $T_{ELD} \sim 250\ (v_{te}^2/v_{||}^2)\ (1/n_{||}^2)$, where $v_{te}/v_{||} \sim 2.5$-3.0. The baseline launch location of 42.5 degrees on the LFS, avoids interference with the passive stabilizer plates, and the $n_{||}$ value of 1.9 led to a higher CD efficiency. The driven current is 1.07 MA, for $n_{||}$ = 1.9. For the HFS the launch location was chosen to be 225 degrees. The launched $n_{||}$ is 1.7, and the maximum driven current is 1.29 MA. In both the reference cases, the $\Delta n_{||}$ = +/- 0.3 at the base, with a sin(x)/x spectrum shape. This is a fairly narrow spectrum, and broader spectra can provide broader CD profiles. The high toroidal field in the FNSF is allowing greater accessibility for lower $n_{||}$ values and deeper penetration of the CD. Specular reflection was assumed in these simulations, although single pass absorption dominated. From Fig. 12, the current deposition ranges from ~ 0.6 to 0.8 for both the LFS and HFS launch, although the HFS launch provides 20% more current. The resulting current drive efficiencies for HFS and LFS cases are 0.043 A/W or 0.26 A/W-m^2 and 0.036 A/W or 0.22 A/W-m^2, respectively.

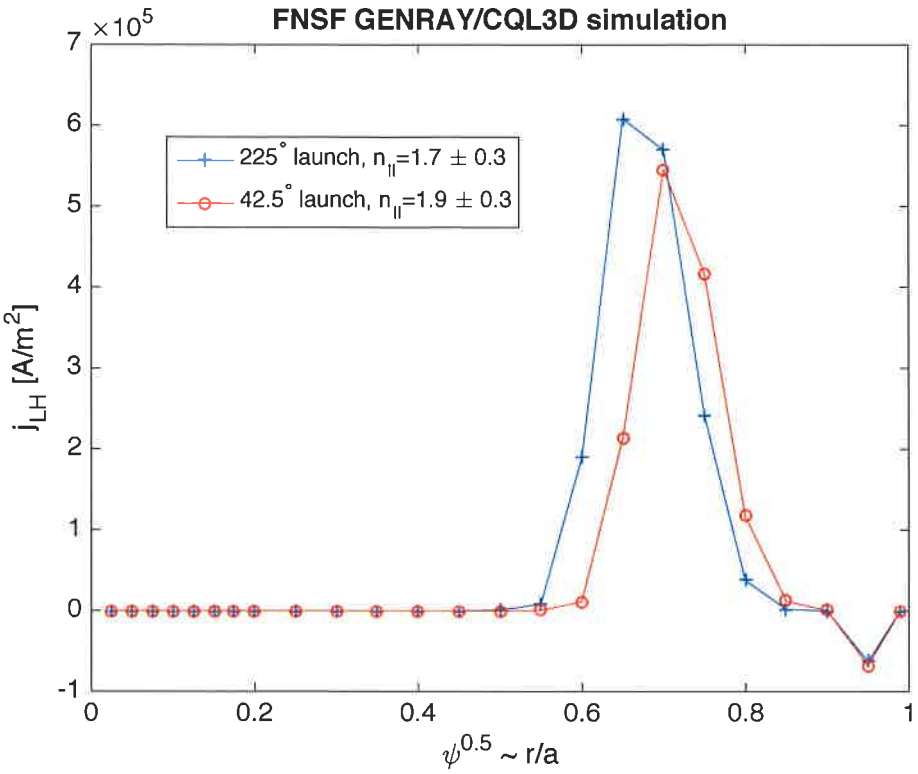

Figure 12. LH driven current in MA for 30 MW of injected power versus the plasma minor radius, for the LFS 42.5 degrees above the outboard midplane and HFS 225 degrees reference cases, from GENRAY-CQL3D analysis.

V.3. Neutral Beam

Neutral beam (NB) heating and current drive can be an important contribution especially when trying to make plasmas at lower beta, where the bootstrap current is as low as ~ 50%. The deposition location of the FWCD (ICRF) is localized on-axis at $\rho < 0.2$, and the LHCD can range from $\rho \sim 0.5$-0.9. In between, the bootstrap current dominates, but is not sufficiently high to provide a decreasing total current density. The NB current profile can be made quite broad, decreasing slowly toward the plasma edge. Here we examine 1 MeV negative ion NBs, like ITER, using the ACCOME NB module [31], which is a Fokker Planck treatment. The NB is oriented to minimize its impact on the blanket sectors by making the tangency radius as close to the inboard plasma edge as possible. The beam footprint is 2.0 m x 0.715 m, and enters through a port at a small angle, making the center of the NB footprint pass through the tangency radius at R = 3.96 m and Z = 0.0. The source is ~ 30 m from the tangency point and elevated 2.0 m. Fig. 13 shows a top and a side view of the NB in the fusion core. The ACCOME simulations show that ~ 1.85 MA can be driven for 50 MW of injected power, giving 0.037 A/W, or (nRI_{NB}/P_{NB}) a CD efficiency of 0.28 A/W-m^2. Fig. 14 shows the NB driven current density as a function of minor radius, along with the bootstrap current, ICRF FW current and total current. The broad deposition is notable. The Z_{eff} value and central density were

2.0 and 1.95×10^{20} /m^3, respectively. Variations were examined to view sensitivities of the NB driven current; at beam particle energy of 750 keV the I_{NB} dropped to 1.6 MA, when the NB source was moved to a height of Z = 0.0, the change in I_{NB} was negligible, and cases with Z_{eff} = 1.5 and 2.5 showed an ~ 5% increase and decrease, respectively. The NBCD has turned out to be critical to achieving 100% non-inductive plasma current due to its ability to "fill-in" the current density profile.

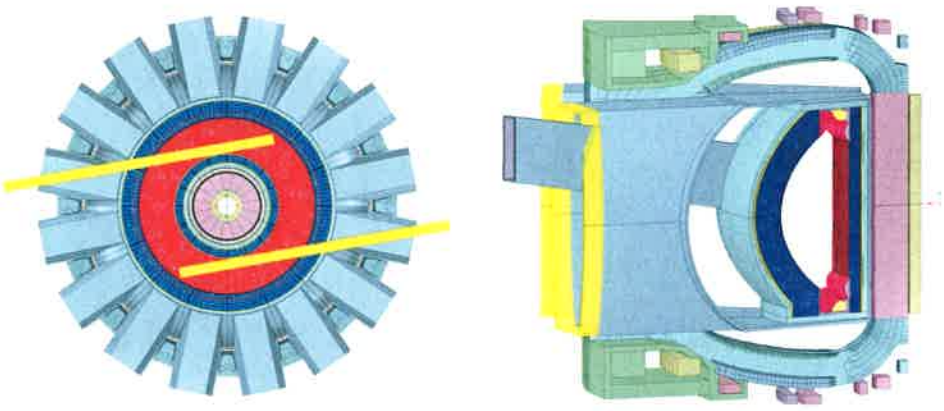

Figure 13. Top view and side view of the neutral beam path and duct, showing the tangency radius near R-a, the impact on the breeding blanket sectors, and how the duct protrudes out through the vacuum vessel port. There is a minor interference with the very end of the port.

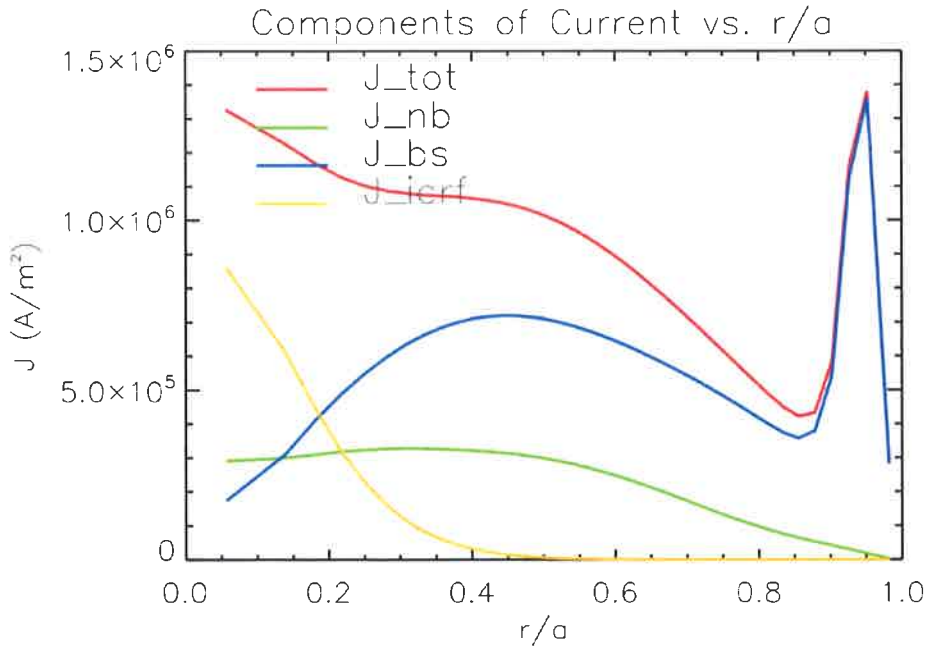

Figure 14. Driven current density for the reference case of 1 MeV negative ion neutral beam (J_nb), 50 MW injected power, with the source at 30 meters from the tangency

radius and elevated by 2.0 m. Also shown are the total (J_tot), bootstrap (J_bs), and ICRF current (J_icrf) profiles, from the ACCOME simulation.

V.4. Electron Cyclotron

The electron cyclotron (EC) was not analyzed for the FNSF parameters, but is scaled from the GENRAY simulations for ARIES-ACT2 [5], and [32] for Korean-DEMO. For the 7.5 T at the plasma center, The frequency is chosen to be ~ 225 GHz, which should provide deposition from 0.1-0.6, scaled by the density and temperature provides efficiencies in the range of 0.008-0.011 A/W for the FNSF, with launching from the outboard side. A maximum of 220 kA is assumed for 20 MW of injected power in the time-dependent simulations. The EC is used primarily for central heating, current profile control, and NTM stabilization.

VI. Physics Impacts on the FNSF and Conclusions

Overall, the FNSF core plasma configuration has a reasonable basis for its successful operation. The demands on energy confinement and beta are low. The low beta limit for the reference configuration of the FNSF, in combination with the power plant relevant high density, has forced a high installed total H/CD power for the facility ~ 120 MW. The H/CD sources were not down-selected because high power demonstrations of all sources does not exist, and there are sufficient issues with all sources to make them vulnerable in the long duration fusion nuclear and plasma regime. Negative ion NB's, LH, and ICRF are found to provide effective CD for the FNSF, and EC is used for profile control due its flexibility in deposition location.

Examining a range of temperature and density profiles shows variations in the alpha power that are not large, leading to fusion gains from 3.6-4.5. The energy confinement requirement in 1.5D analysis is higher than predicted by the systems code by 10-20%, giving H_{98} ~ 1.1-1.2. The plasma energy confinement requirements are generally modest, however the predictions of the GLF23 theory based model are low, and this area requires more detailed assessments to make projections into the FNSF operating regime. The pedestal height was determined from EPED, resulting in $T_{e,ped}$ ~ 4.3 keV and $T_{i,ped}$ ~ 4.0 keV, for the reference density and Z_{eff} ~ 1.8.

The equilibrium analysis shows that the CS coil has large currents in the nominal configuration, giving rise to high current densities. This is the result of a large neutron shielding build on the inboard side and a thick TF coil. Subsequently, the shielding was found to provide lower fluence and heating than targeted, which could provide ~ 10 cm increase to the CS coil radius. A HTSC conductor is likely to be the best solution to obtain higher current density and superior strength in the solenoid geometry, compared to LTSC in CICC configuration. Another solution described in [33] is to pursue a bucked and wedged mechanical configuration (CS/TF), which allows the CS to move outward and reduce its currents sufficiently for a LTSC solution.

Ideal MHD has confirmed the no-wall beta estimates used in the systems analysis and reported for the ARIES-ACT2 power plant study [5], however, experimental operation of plasmas right at or near the no-wall beta is required to understand the plasma potential for long duration sustainment. In addition, kinetic stabilization or rotation with error field correction and RWM feedback could provide the means to operate at higher betas. Projecting these phenomena to the FNSF regime is needed. A conducting wall placed on the outboard side at distances from the plasma boundary ranging from 0.33a to 0.74a can increase the reachable beta limit. This shell would be made of tungsten for its good electrical conductivity and high melting temperature, but the impact of currents driven it during a disruption current quench require attention, and are being examined [17].

Each of the H/CD sources have an established, or anticipated for ITER, power density through the first wall. This, in combination with the CD efficiency of each of the sources, impacts the facility since it requires a penetration through the breeding blanket, and therefore reduces tritium production. The power densities assumed here are 20 MW/m^2 for a PAM LH launcher, 10 MW/m^2 for a 4-strap ICRF antenna, 25 MW/m^2 for neutral beams, and 20-40 MW/m^2 (depending on launch structure). The nuclear analysis of sectors with each of the H/CD penetrations included allows us to determine the impact on the tritium breeding ratio [34], and even with this H/CD layout a TBR ~ 1.07 was achieved. The reference H/CD combination calls for 2 NB's at 25 MW each, and each having a 2.0 m x 0.715 m beam footprint. The LH on the LFS requires 30 MW, and the single launcher grill has dimensions of 0.85 m x 1.75 m. The ICRF on the outboard midplane requires 20 MW, and the single launcher is 1.2 m x 1.7 m. Finally, the EC installed is 20 MW for current profile control, and the launching structure is 0.5 m x 1.35 m, depending where it is located on the outboard side. The total H/CD wall area required is ~ 7 m^2, and with some structure and standoff, this grows to about 8 m^2. There are many issues associated with each of the H/CD schemes ranging from neutron exposure of the NB ion source and acceleration grids to materials and plasma coupling for the ICRF and LH systems. ITER demonstrations of these sources in a burning plasma at 10's of MW level are needed to assess their viability.

Acknowledgement

Work supported by DOE contracts DE-AC02-09CH11466 for PPPL, DE-AC52-07NA27344 for LLNL, DE-FC02-99ER54512 for MIT, DE-AC05-00OR22725 for ORNL.

References

[1] C. E. Kessel et al, "Overview of the Fusion Nuclear Science Facility, a Credible Break-in Step on the Path Fusion Energy", Fusion Engr. Des., THIS ISSUE.

[2] R. W. Conn and F. Najmabadi, "ARIES-I, A Steady State First Stability Tokamak Reactor with Enhanced Safety and Environmental Features", Nucl Fusion Supplement, **3,** (1991), 659.

[3] S. C. Jardin et al, Fusion Engr. Des., **38**, (1997), 27.

[4] F. Najmabadi et al, Fusion Engr Des., **80**, (2006), 3.

[5] C. E. Kessel et al, Fusion Sci. Technol., **67**, (2015), 75 & 220.

[6] S. C. Jardin et al, J. Comput. Phys., **66**, (1986), 481.

[7] W. M. Tang, Nucl. Fusion, **26**, (1986), 1605.

[8] Jardin TSC ohmic

[9] G. M. Staebler et al, Nucl. Fusion, **37**, (1995), 287.

[10] J. E. Kinsey et al, Phys. Plasmas, **12**, (2005), 052503.

[11] P. Snyder et al, Plasma Phys. Control. Fusion, **46**, (2004), A131.

[12] O. Sauter and C. Angioni, Phys. Plasmas, **6**, (1999), 2834.

[13] C. E. Kessel et al, Fusion Engr. Des., **80**, (2006), 63.

[14] Y. Martin et al, J. Physics Conf. Ser., **123**, (2008), 012033.

[15] C. E. Kessel et al, Fusion Sci Technol., **64**, (2013), 440.

[16] W. Fundamenski et al, Nucl. Fusion, **45** (2005), 950.

[17] J. P. Blanchard et al, "Effect of ELMs and Disruptions on FNSF Plasma Facing Components", Fusion Engr. Des., THIS ISSUE.

[18] J. DeLucia et al, J. Comput. Phys., **37**, (1980), 183.

[19] J. M. Greene et al, Nucl. Fusion, **21**, (1981), 453.

[20] R. C. Grimm et al, J. Comput. Phys., **49**, (1983), 94.

[21] A. Garofalo et al, Nucl. Fusion, **47**, (2007), 1121.

[22] Y. Liu et al, Pjys. Plasmas, **15**, (2008), 092505.

[23] I. T. Chapman et al., Plas. Phys. Control. Fusion, **51**, (2009), 055015.

[24] J. R. Wilson et al, Phys. Rev. Lett., **75**, (1995), 842.

[25] D. F. H. Start et al, Phys. Rev. Lett., **80**, (1998), 4681.

[26] M. Brambilla, Plas. Phys. Control. Fusion, **41**, (1999), 1.

[27] J. C. Wright et al, Phys. Plasmas, **11**, (2004), 2473.

[28] R. W. Harvey and M. G. McCoy, Proc. IAEA Technical Committee Mtg. Advances in Simulation and Modeling of Thermonuclear Plasmas, Montreal, Quebec, Canada, 1993, p 489, USDOC NTIS Doc. No. DE93002962, IAEA (1993).

[29] A. Smirnov et al, Proc. 15th Workshop ECE and ECRH, p 301, World Scientific (2009).

[30] G. M. Wallace et al, Fusion Engr. Des., THIS ISSUE

[31] R.S. Devoto et al, Nucl. Fusion, **32** (1992) 773.

[32] D. Mikkelsen et al, "Heating and Current Drive Examination for the Korean DEMO", to be submitted to Fusion Engr. Des.

[33] Y. Zhai et al, "Magnet Design Study for the Fusion Nuclear Science Facility". Fusion Engr. Des., THIS ISSUE.

[34] A. Davis et al, "Neutronics Aspects of the FESS-FNSF", Fusion Engr. Des., THIS ISSUE.

PPPL PRINCETON PLASMA PHYSICS LABORATORY

Princeton Plasma Physics Laboratory
Office of Reports and Publications

Managed by
Princeton University

under contract with the
U.S. Department of Energy
(DE-AC02-09CH11466)

P.O. Box 451, Princeton, NJ 08543
Phone: 609-243-2245
Fax: 609-243-2751

E-mail: publications@pppl.gov

Website: http://www.pppl.gov